Geophysical Journal International

Geophys. J. Int. (2022) **229,** 1870–1880
Advance Access publication 2022 February 04
GJI Seismology

https://doi.org/10.1093/gji/ggac031

Wavefield reconstruction and wave equation inversion for seismic surface waves

A. Shaiban,* S.A.L. de Ridder † and A. Curtis

School of GeoSciences and Grant Institute of Earth Science, University of Edinburgh, Edinburgh EH93FE, UK. E-mail: ali.shaiban.5@aramco.com

Received 2022 January 21; in original form 2021 November 15

SUMMARY

Surface waves are a particular type of seismic wave that propagate around the surface of the Earth, but which oscillate over depth ranges beneath the surface that depend on their frequency of oscillation. This causes them to travel with a speed that depends on their frequency, a property called dispersion. Estimating surface wave dispersion is of interest for many geophysical applications using both active and passive seismic sources, not least because the speed–frequency relationship can be used to infer the subsurface velocity structure at depth beneath the surface. We present an inversion scheme that exploits spatial and temporal relationships in the scalar Helmholtz (wave) equation to estimate dispersion relations of the elastic surface wave data in both active and passive surveys, while also reconstructing the wavefield continuously in space (i.e. between the receivers at which the wavefield was recorded). We verify the retrieved dispersive phase velocity by comparing the results to dispersion analysis in the frequency-slowness domain, and to the local calculation of dispersion using modal analysis. Synthetic elastic examples demonstrate the method under a variety of recording scenarios. The results show that despite the scalar approximation made to represent these intrinsically elastic waves, the proposed method reconstructs both the wavefield and the phase dispersion structure even in the case of strong aliasing and irregular sampling.

Key words: Computational seismology; Seismic noise; Surface waves and free oscillations.

1 INTRODUCTION

Geophysical methods are often used to infer Earth's internal structure. In seismology this usually involves the analysis of two main types of seismic energy propagation: body and surface waves. Body waves consist of energy that travels through the Earth's interior while surface waves are attributed to the energy that is trapped near the Earth's surface. Surface waves are measured in active surveys (Peiming *et al.* 2016) as well as passive surveys (Shapiro *et al.* 2005; Curtis *et al.* 2006; De Ridder & Dellinger 2011) and are used for different applications such as inferring the structure of Earth's crust and mantle (Trampert & Woodhouse 1995; Curtis *et al.* 1998) or for near-surface imaging and engineering (Jones 1958; Socco *et al.* 2010).

Surface waves travel with a speed that depends on frequency, a property called dispersion. Given the dispersion relation of a medium, it is possible to estimate its subsurface velocity structure (Xia *et al.* 1999). The commonly used methods to estimate dispersion of surface waves include frequency wavenumber (*f–k*) or frequency slowness (*f–p*) analysis (McMechan & Yedlin 1981) using long seismic arrays. These methods provide an averaged dispersion curve across a long array, and make the implicit assumption of a laterally invariant (i.e. horizontally layered) medium below the array (Foti *et al.* 2000). Alternatively, path-averaged dispersion may be estimated between a point-source and a single receiver by analysing the arrival time of different wave frequencies and dividing by the estimated source–receiver distance (Trampert & Woodhouse 1995; van Heijst & Woodhouse 1997). Either method therefore provides spatially averaged rather than local dispersion at each geographical location. Surface wave tomography is then used to spatially localize dispersion. This involves picking many dispersion relations (usually called dispersion curves) from different *f–k* records and inverting their spatial averaging in order to estimate a map of surface wave dispersion at each location using phase velocity (Nicolson *et al.* 2012; Galetti *et al.* 2016) or group velocity (Levshin *et al.* 2018).

Seismic data are usually measured at discrete spatial locations. It is often also of interest to know the wavefield between recording locations for a variety of signal processing and imaging techniques, in which case wavefield interpolation or reconstruction is necessary. A variety of methods exist to reconstruct a wavefield such

*Now at: Saudi Aramco, Dhahran, Saudi Arabia
†Now at: School of Earth and Environmental Sciences, University of Leeds, Leeds LS29JT, United Kingdom

as frequency–space (*f*–*x*) interpolation (Spitz 1991), wave equation based interpolation (Ronen 1987) and Fourier reconstruction (Zwartjes & Sacchi 2006), some of which can be used for aliased and non-uniformly recorded data. Zhan *et al.* (2018) presented a wavefield compressive sensing method for reconstructing the wavefield of the surface waves. They showed that the method is capable of yielding better results in velocity estimation methods such as Helmholtz tomography or wavefield gradiometry. The formulation was based on a plane wave representation of surface waves, and was demonstrated to enhance velocity estimation using methods that require spatial derivatives of the wavefield to be estimated across irregular arrays of receivers. In another approach, Lehujeur & Chevrot (2020) proposed to extract and isolate coherent wave fronts that travel across seismic arrays using an iterative matched filtering method and then deriving phase velocities using eikonal tomography.

Gradiometry is another approach to extract useful information from surface waves in active or ambient seismic records. The term gradiometry refers to the explicit use of wavefield gradients in space and time to estimate properties of the wavefield or the medium. Curtis & Robertsson (2002) first proposed to measure first- and second-order spatial derivatives of the recorded wavefield in order to invert the equation of motion for properties of the medium. To estimate vertical derivatives, they used volumetric recordings (where one of the receivers is buried beneath the surface) and obtain gradient estimates using finite-difference methods. They used these derivatives to invert the elastic wave equation for the effective near-surface *P* and *S* velocities, a method they called wave equation inversion. Their derivation holds for any incoming wavefield, including ambient noise. Langston (2007a) used the first-order spatial and temporal gradients of a plane-wave arrival to estimate the horizontal wave slowness. This method was extended for 2-D surveys, which provided extra information about azimuthal radiation patterns (Langston 2007b). Both methods of Langston (2007a, b) are based on the assumption that there is a single propagating wave, so the formulation does not hold for interfering wave modes such as are found in wavefields consisting of ambient seismic noise. Edme & Yuan (2016) applied the gradiometry method described by (Langston 2007a, b) to estimate dispersion curves for surface waves using ambient noise data. They introduced statistical methods to detect and avoid overlapping waves in an attempt to satisfy the assumption of non-interference.

De Ridder & Biondi (2015) proposed to invert the scalar wave equation to estimate phase velocities of surface waves using ambient noise data recorded across the Ekofisk field in the Norwegian North Sea. Their formulation is based on a single frequency of propagation. To avoid dispersion related effects, they first apply a narrow bandpass around each desired frequency. Then, the analysis is repeated for different frequencies to estimate the dispersion curves. Unlike seismic interferometry, their method does not require long recording times but assumes that there is a single mode of surface wave propagation (i.e. that the fundamental mode dominates over the amplitude of higher modes). This method was extended to include both isotropic and anisotropic media by De Ridder & Curtis (2017) using an elastodynamic wave equation with anisotropic phase velocity. The results of De Ridder & Biondi (2015) and De Ridder & Curtis (2017) matched results obtained using conventional cross-correlation tomography studies across the same field, thus verifying the methodology.

Full waveform inversion (FWI) is an optimization technique that calculates synthetic waveforms from a given subsurface model and then updates the model to minimize the difference between these synthetic waveforms and those observed. The update of the subsurface model is done by projecting the residual difference between the waveforms into the gradient that defines the best direction to update the model (Tarantola 1984). Most of the current formulations of FWI involve estimating both forward and adjoint wavefields.

van Leeuwen & Herrmann (2013) proposed a partial differential equation (PDE) constrained method that enlarges the search space by estimating the wavefield everywhere in the model while inverting for the medium parameters which may mitigate the issue of converging to local rather than global optima in classic FWI formulations. This is done by introducing a penalty term in the objective function to make the wavefield satisfy the wave equation. The optimization problem composed of two coupled optimization objectives to find (i) a wavefield satisfying the wave equation PDE, and (ii) a structural model governing the PDE such that the wavefield matches observations. Zhang & Alkhalifah (2019) proposed to use FWI to maximize the similarity of the phase velocity spectrum (*f*–*v*) between the observed and predicted waveforms of all Rayleigh wave. Their methodology allowed dispersion curves of all Rayleigh-wave modes to be used without the need for manual picking to invert for *S*-wave velocity structure. Recent developments in machine learning employs training neural networks as a proxy process for tomography posed as a PDE constrained optimization process (bin Waheed *et al.* 2021).

de Ridder & Maddison (2018) used a similar method to the PDE constrained inversion for a wavefield inversion of ambient seismic noise. One key difference is that the inversion for ambient noise is formulated with unknown sources by introducing a boundary condition to the inversion algorithm where sources are known to be negligible inside a subdomain. The synthetic examples showed that the inversion scheme retrieved a good velocity model and reconstructed a reasonable estimate of the ambient noise wavefield. Effective source functions are projected to the boundaries of the domain. However, the formulations that they used were limited to the time-domain data.

In this paper, we extend the approach of de Ridder & Maddison (2018) to the case where we use the Helmholtz equation in the frequency domain with a frequency-dependent velocity to approximate the horizontal propagation of elastic surface waves. We perform an iterative two-step inversion which in each iteration first reconstructs the wavefield that best matches our observations using an estimate for the phase velocity model, after which we update the phase velocity model using a local wave equation inversion of the wavefield.

We test the proposed method using an example representing an elastodynamic wavefield (including surface waves) generated by a single active source, and an example of ambient noise (dominated by surface waves) excited by many seismic sources. To demonstrate the effectiveness of our method, we compare the dispersion curves from our algorithm to the ones estimated using the *f*–*p* method. Unlike the *f*–*p* method which assumes lateral homogeneity, the results of our method recovers both laterally heterogeneous velocities and their corresponding wavefields.

2 METHODOLOGY

The Helmholtz equation with frequency-dependent velocity describes wave motion in a dispersive medium. It has been used to describe the far-field motion of surface waves in an elastic medium (Aki & Richards 2002) and underlies many methods that estimate surface wave phase velocity maps (Aki 1957; Wielandt 1993). The

1-D form can be written as follows:

$$c^2(x,\omega)\partial_x^2\, u(x,\omega) + \omega^2\, u(x,\omega) - s(x,\omega) = 0 \tag{1}$$

where $u = u(x, \omega)$ is the scalar pressure or particle displacement field at spatial location x and angular frequency ω, $c = c(x, \omega)$ is the phase velocity and $s = s(x, \omega)$ is the source function.

We aim to solve for the wavefield of the surface waves that satisfy eq. (1) and to solve for a velocity model such that the wavefield matches the observation in a joint inversion algorithm. We refer to our method as *full wavefield inversion* (FWFI) since we reconstruct the full wavefield while also estimating medium properties that control the wave phenomena. The match of the wavefield against a finite number of observations involves a sampling function and norm over a discrete space. Therefore, the remainder of the paper is more easily expressed after discretizing the wavefield and sources.

The fields, u, s, and medium parameters c are discretized on a finite basis as a regular grid with spacing Δx and frequency interval $\Delta\omega$. The spatial derivatives are approximated by central finite differences. Bold terms will now represent discretized quantities over space and frequency ($\mathbf{x}$, $\boldsymbol{\omega}$) arranged into a 1-D array, where $\mathbf{x}$ contains the set of locations (the spatial basis) and $\boldsymbol{\omega}$ contains the set of frequencies (the frequency basis) on which the field $\mathbf{u}$ is defined. For simplicity we define $\mathbf{m} = \mathbf{c^2}$. The spatial derivative operator (acting on each frequency) can now be arranged into a matrix $\mathbf{L}$, acting as a matrix-vector operator on the field $\mathbf{u}$. The matrix-vector system representing the discretized version of eq. (1) can be expressed in two different linear forms:

$$\mathrm{diag}\{\mathbf{m}\}\mathbf{L}\mathbf{u} + \mathrm{diag}\{\omega^2\}\mathbf{u} - \mathbf{s} = 0 \tag{2}$$

and

$$\mathrm{diag}\{\mathbf{L}\mathbf{u}\}\mathbf{m} + \mathrm{diag}\{\omega^2\}\mathbf{u} - \mathbf{s} = \mathbf{0} \tag{3}$$

where $\mathrm{diag}\{\mathbf{m}\}$ is a square matrix with $\mathbf{m}$ on the diagonal and zero elsewhere. The frequency-spatial sampling operator $\mathbf{K}$ can likewise be written as a matrix, K_{ij}, which is equal to one for the spatial locations and frequencies at which we have a wavefield measurement, and it is zero where we do not. Our discrete sampling of the wavefield therefore results in the following condition on wavefield $\mathbf{u}$:

$$\mathbf{K}\mathbf{u} = \mathbf{d} \tag{4}$$

where $\mathbf{d}$ represents the discrete wavefield measurements.

The general problem we address in this manuscript is to solve for a wavefield satisfying the governing PDE, while also solving for the medium parameters which govern that PDE simultaneously, which can be expressed as the following optimization problem:

$$J(\mathbf{u},\mathbf{m}) = \epsilon_1 \left\| \mathbf{K}\mathbf{u} - \mathbf{d} \right\|_2^2 + \epsilon_2 \left\| \mathbf{W}[\mathrm{diag}\{\mathbf{m}\}\mathbf{L}\mathbf{u} + \mathrm{diag}\{\omega^2\}\mathbf{u} - s] \right\|_2^2 \tag{5}$$

where the second term can be written with either of the linear forms of the Helmholtz equation. The solutions for the wavefield and medium parameters are found as

$$\mathrm{argmin}_{\mathbf{u},\mathbf{m}}\, J(\mathbf{u},\mathbf{m}) \rightarrow \hat{\mathbf{u}}, \hat{\mathbf{m}} \tag{6}$$

However, we follow de Ridder & Maddison (2018) and do not solve the wavefield and the phase velocity simultaneously but perform a two-step iterative procedure: in each iteration, we first estimate the full wavefield using the wavefield reconstruction inversion. Second, we directly invert the wave equation for the phase velocity using the wave equation inversion. The process of our methodology is illustrated in a sketch in Fig. 1. Next, we introduce each step separately.

2.1 Wavefield reconstruction inversion (WRI)

We measure seismic wavefield at discrete spatial locations, so we introduce wavefield reconstruction inversion to reconstruct the wavefield between measurement points. The motivation here is to enhance the estimates of the spatial derivatives of the wavefield required to estimate the phase velocity model using wave equation inversion. We use the first linear form, eq. (2), of the Helmholtz equation. We introduce a masking operator $\mathbf{W}$ in space and frequency which selects an area where we will reconstruct the wavefield. For this, we use both eqs (2) and (4) in addition to an estimate of the model parameter $\mathbf{m} = \mathbf{m}'$. In the minimization scheme, two objective functions measuring the squared misfit to eqs (2) and (4) are weighted by a scaling parameter, denoted by ϵ_1. We seek a least-squares solution for the wavefield $\mathbf{u}$ by combining eqs (2) and (4) and the mask $\mathbf{W}$ using the following cost function:

$$J_{wri}(\mathbf{u}) = \left\| \mathbf{K}\mathbf{u} - \mathbf{d} \right\|_2^2 + \epsilon_1 \left\| \mathbf{W}[\mathrm{diag}\{\mathbf{m}'\}\mathbf{L}\mathbf{u} + \mathrm{diag}\{\omega^2\}\mathbf{u} - s] \right\|_2^2 \tag{7}$$

In practise, we find that as long as ϵ_1 is chosen small enough to balance the terms such that the data fitting term is relatively more important than the physics enforcement term, the particular choice of ϵ_1 does not impact the final result but affects the convergence rate of the iterative scheme. We also select a frequency-spatial domain such that $\mathbf{W} * \mathbf{s} = 0$: that is, we assume that the source function can be neglected within the selected domain for inversion. For a given estimate of the model parameter $\mathbf{m}'$, we find the optimal wavefield $\hat{\mathbf{u}}$ by the following:

$$\mathrm{argmin}_{\mathbf{u}}\, J_{\mathrm{wri}}(\mathbf{u}) \rightarrow \hat{\mathbf{u}} \tag{8}$$

2.2 Wave equation inversion (WEI)

After reconstructing the wavefield, we use WEI (Curtis & Robertsson 2002) to estimate the velocity model. We use the second linear form, eq. (3), of the Helmholtz equation to estimate phase velocities $\mathbf{m}$ using the estimated wavefield $\hat{\mathbf{u}}$ from the first step. We introduce a second-order Tikhonov regularization term to favour solutions with lower model roughness. This is based on geological prior information that phase velocities tend to change reasonably smoothly across both space and frequency. This regularization term is expressed by fitting the objective:

$$\mathbf{A}\mathbf{m} = [\mathbf{A}_1 + \epsilon_2\mathbf{A}_2]\,\mathbf{m} = \mathbf{0} \tag{9}$$

The matrices $\mathbf{A_1}$ and $\mathbf{A_2}$ represent smoothing in space and frequency, respectively, and contain second-order finite-difference stencils over space and frequency points, which calculate roughness of the model parameters $\mathbf{m}$. ϵ_2 is the scaling factor used to control the weight of smoothing in frequency versus space. Similarly to WRI, we use a mask $\mathbf{M}$ in space and frequency for WEI. The mask $\mathbf{M}$ is smaller than the mask $\mathbf{W}$ used in WFI so that the finite-difference stencils of WEI do not extend outside of the region selected for WRI. Similarly to the way we reconstruct the wavefield in WRI, we define the cost function as follows:

$$J_{\mathrm{wei}}(\mathbf{m}) = \left\| \mathbf{M}[\mathrm{diag}\{\mathbf{L}\hat{\mathbf{u}}\}\mathbf{m} + \mathrm{diag}\{\omega^2\}\hat{\mathbf{u}} - \mathbf{s}] \right\|_2^2 + \epsilon_3 \left\| \mathbf{A}\mathbf{m} \right\|_2^2 \tag{10}$$

By analogy to WRI, we choose a masking operator $\mathbf{M}$ such that $\mathbf{M} * \mathbf{s} = 0$. For a given estimate of the wavefield $\hat{\mathbf{u}}$, we find the optimal model parameter by:

$$\mathrm{argmin}_{\mathbf{m}}\, J_{\mathrm{wei}}(\mathbf{m}) \rightarrow \hat{\mathbf{m}} \tag{11}$$

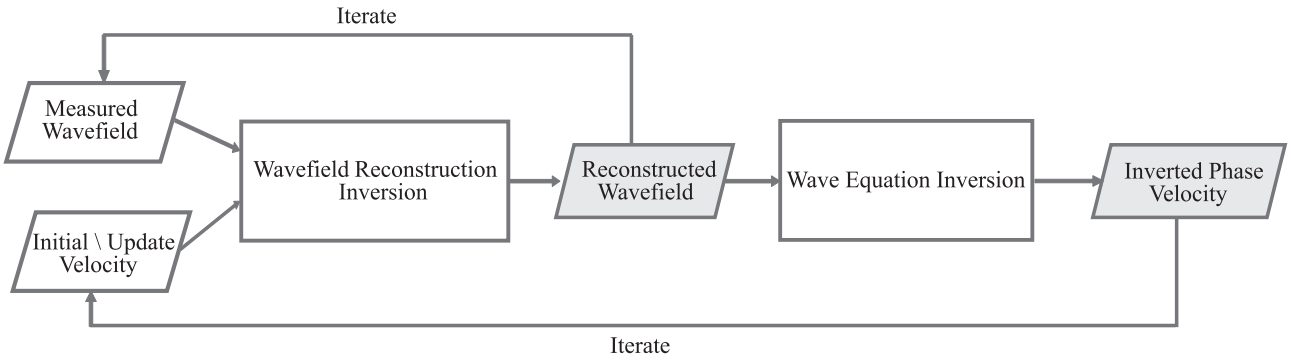

Figure 1. A sketch illustrating our proposed method. In the first iteration, the input to the method are the measured wavefield and an initial velocity model. The iterated, nonlinear wavefield reconstruction inversion outputs a reconstructed wavefield which is then used as input for the linear wave equation inversion to output a new estimate of the phase velocity. In subsequent iterations, the newly reconstructed wavefield and the new estimate of the phase velocity are used as an input for the methodology. We iterate until we have a convergence.

2.3 Full wavefield inversion (FWFI)

We iterate between WRI and WEI to find an optimal solution for both $\mathbf{m}$ and $\mathbf{u}$ upon convergence. To reconstruct the wavefield in the first iteration, we must have a starting velocity model. This model estimate will be updated in subsequent iterations. We solve the inversion by employing a conjugate gradient algorithm for WRI starting from the trivial solution $\mathbf{u_0} = \mathbf{0}$. In subsequent iterations, we use the reconstructed wavefield of the previous iteration as a starting model in the conjugate gradient algorithm for WRI. WEI is solved using the same algorithm. The joint inversion in iteration N is thus defined to find optimal model parameter $\mathbf{m}_N$, and best reconstructed wavefield $\mathbf{u}_N$, as shown in the following scheme:

$$\begin{aligned}\mathbf{u}_0, \mathbf{m}_0 \rightarrow \text{argmin}_{\mathbf{u}}\, J_{\text{wri}}(\mathbf{u}) \rightarrow \mathbf{u}_1 \rightarrow \\ \rightarrow \text{argmin}_{\mathbf{m}}\, J_{\text{wei}}(\mathbf{m}) \rightarrow \mathbf{m}_1 \rightarrow \\ \rightarrow \text{argmin}_{\mathbf{u}}\, J_{\text{wri}}(\mathbf{u}_1) \rightarrow \mathbf{u}_2 \rightarrow \\ \rightarrow \ldots \rightarrow \mathbf{u}_N \rightarrow \\ \rightarrow \text{argmin}_{\mathbf{m}}\, J_{\text{wei}}(\mathbf{m}) \rightarrow \mathbf{m}_N\end{aligned} \tag{12}$$

2.4 WEI regularization parameters

There exists a trade-off between the scaling parameters used for the second-order Tikhonov regularization in space and frequency. To choose appropriate parameters we follow a similar approach to Nicolson *et al.* (2014) where the normalized root mean squared (rms) data residual, which is a dimensionless quantity, is computed for different combinations of regularization parameters. For our research, we tried different combinations of ϵ_2 and ϵ_3 and then calculate the rms of the data residual for each combination as follows:

$$E = \sqrt{\frac{1}{N}\sum_{i=1}^{N}\frac{[\mathbf{d}_i - \mathbf{u}_i]^2}{\sigma_i^2}} \tag{13}$$

where E is the rms of the data residual, N is the number of samples, $\mathbf{d}_i$ is the input data at location i, $\mathbf{u}_i$ is the reconstructed wavefield at location i, and σ_i is the covariance of the input data at location i. In our case, σ is unknown for the input data and we set it equal to 1, thus assuming that the data units are chosen appropriately given the data accuracy. We expect that E would be minimum for a reasonable combination of ϵ_2 and ϵ_3. Following Nicolson *et al.* (2014), the approach that we use to choose the right frequency and spatial smoothing for WEI is as follows; for combinations of ϵ_2 and ϵ_3 that are too low, the inverted velocity is under-regularized resulting in clear ringing in the inverted phase velocity so such combinations are discarded. For combinations that are too large, the inverted velocity would be over-regularized, would not fit the data, and these are also discarded. For combinations that are in between, we choose the combination for which E is minimum, but recognize that ϵ_2 and ϵ_3 are likely to trade off so the choice is always subjective.

3 ACTIVE SEISMIC EXAMPLE

Fig. 2 illustrates the elastic properties overlain with the acquisition geometry, and the results of elastic synthetic wavefield modelling as performed for the test examples used in this paper. Fig. 2(a) represents the acquisition geometry for a step-like structure over a half-space. This is suitable for testing because a vertical step includes all wavenumbers and hence it is demanding in terms of horizontal resolution. The p-wave velocity is $\sqrt{3}$ times the shear wave velocity in order to represent a Poisson solid medium where λ equals to μ. In this example, we keep the density constant at 1000 kg m^{-3}. We model an elastic wavefield using finite difference methods with one source to the left as shown in Fig. 2(a) and (separately) another source to the right of the model. The elastic wavefield is dominated by surface waves and other modes of waves such as reflected and refracted body waves are also present. The simulated wavefield is recorded in the time domain as shown in Fig. 2(b) but our formulation is in the temporal frequency domain. Therefore, we first apply Fourier transform to the recorded wavefield as shown in Fig. 3(a).

Fig. 3 illustrates the wavefield results of FWFI. Where, Fig. 3(a) shows the true surface wave wavefield in the frequency domain that results from using the left shot in the survey shown in Fig. 2(a). Fig. 3(b) displays the input to FWFI which is the discretely sampled data at a spatial sampling rate of 25 m (which is above the average Nyquist sampling rate for both sides of the model). Figs 3(c) and (d) show the reconstructed wavefield after 50 iterations and the difference between the true elastic wavefield and the reconstructed wavefield, thus demonstrating that FWFI reconstructs the surface wavefield reasonably well. The difference between the true and estimated wavefield is transformed to time domain shown in Fig. 4(b) to illustrate that parts of the wavefield not matched by WRI are mainly the higher order modes and body waves. Note, the difference is small inside the selected area shown by the red box, which represents the frequency-spatial mask applied within the inversion. The spatial sampling rate in Figs 3(a), (c) and (d) is 5 m.

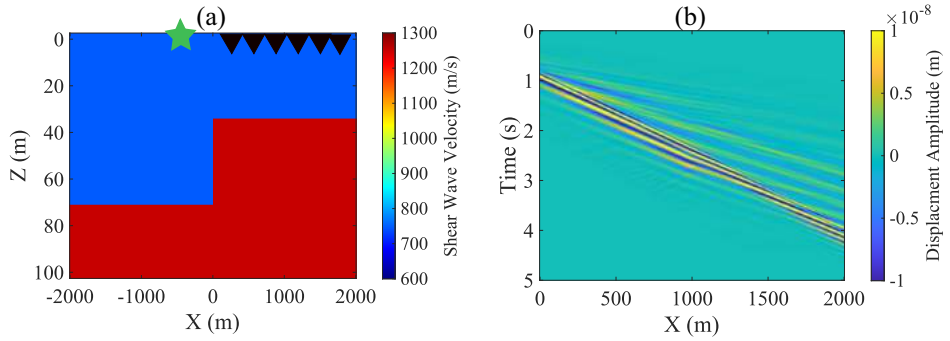

Figure 2. Acquisition geometry and modelling results. (a) Is the shear velocity model we used to generate experimental data. The star shows the seismic source while the triangles show the location of the receiver array. (b) The elastic modelling result in the time domain for the acquisition scenario in (a). The amplitude is proportional to the source function.

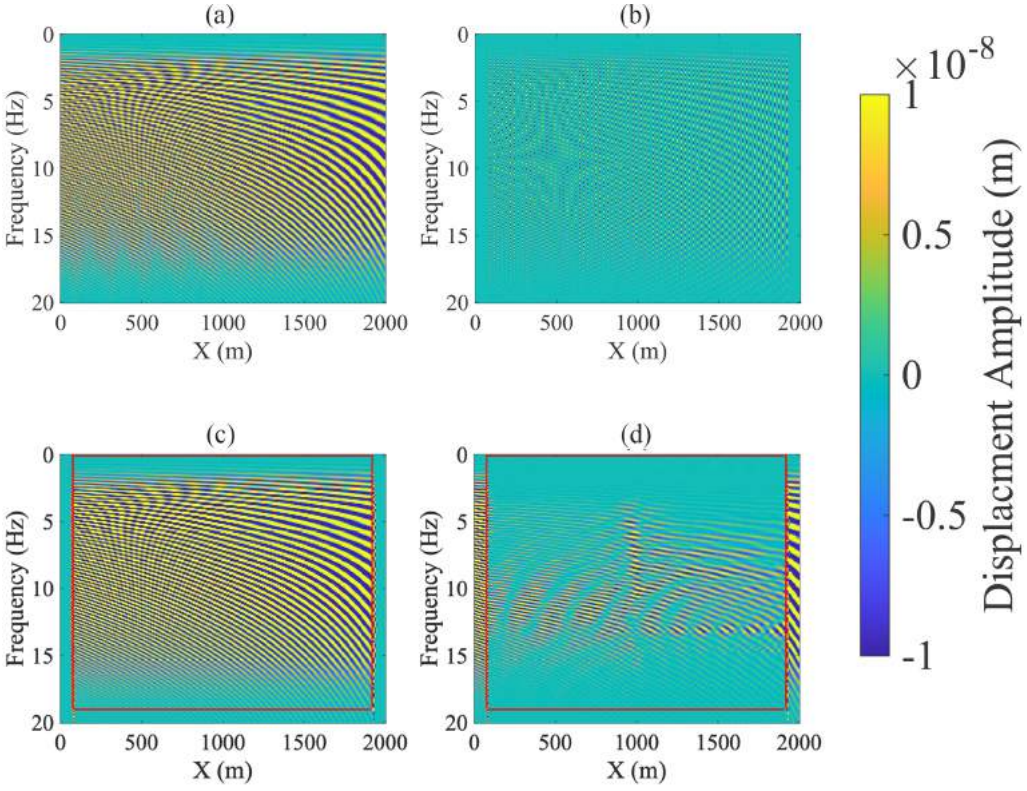

Figure 3. FWFI wavefield results for an active seismic scenario. (a) True modelled wavefield in the space–frequency domain as obtained from the first scenario in Fig. 2(a). (b) The decimated data input to WFI sampled every 25 m. (c) Wavefield estimated by FWFI after 50 iterations. (d) Difference between true and estimated wavefields. The red box in (d) shows the zone where we inverted for phase velocities. Note, spatial sampling intervals are 5 m in panels (a), (c) and (d), and 25 m in panel (b).

Fig. 5 shows the results of WEI for this example. Fig. 5(a) represents the starting velocity model which is a homogeneous dispersive velocity model. Fig. 5(b) shows the retrieved dispersive phase velocity model after 50 iterations in which the step structure is reasonably well resolved. To verify the retrieved phase velocity models, we calculated dispersion images using an *f–p* transform (McMechan & Yedlin 1981) of the horizontal structure on the left, and separately of the horizontal structure on the right-hand side of Figs 2(c) and (d). In Figs 5(c) and (d), we select two phase velocity profiles from both left- and right-hand sides of the retrieved dispersive velocity model (location indicated by dashed lines in Fig. 5b) and overlain with *f–p* dispersion images of these profiles as displayed in Figs 5(c) and (d). Note that the retrieved velocity profiles nicely match the fundamental mode dispersion.

3.1 Choice of regularization parameters

The choice of regularization parameters impacts the retrieved dispersive phase velocity model. There exists a range of possible combinations of the frequency and spatial smoothing parameters. Therefore, we applied the proposed method to find suitable regularization parameter values for ϵ_2 and ϵ_3. We ran a number of combinations of the regularization parameters and calculate E in eq. (13) for each combination with results shown in Fig. 6. The combinations to the left of the purple curves appear under-regularized as the structure oscillates in space; these models are discarded. Similarly, the combinations to the right of the green curve appear over-regularized because there are less regularized models that fit the data equally well or better; the application of more smoothing is equivalent to

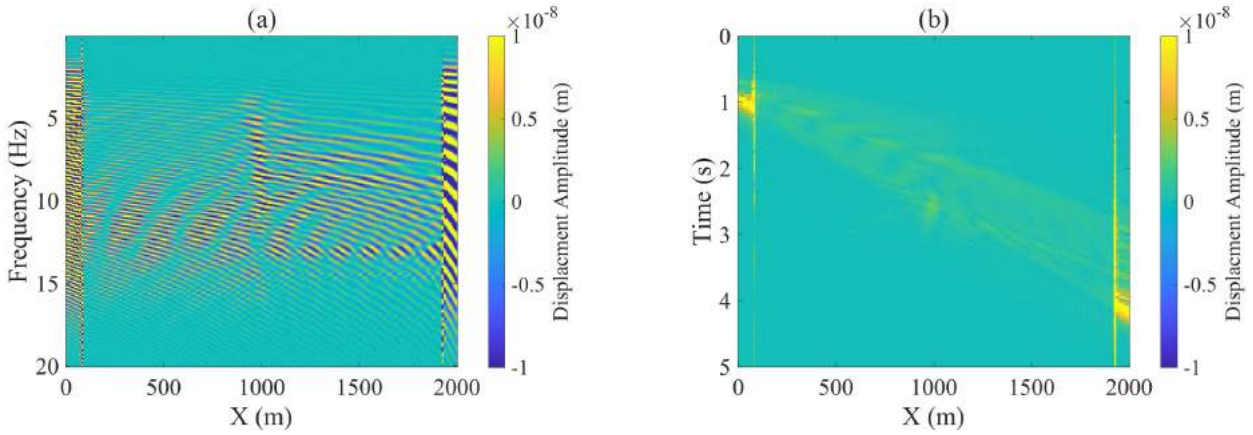

Figure 4. Difference between true and estimated wavefields in (a) frequency domain which transformed to (b) time domain.

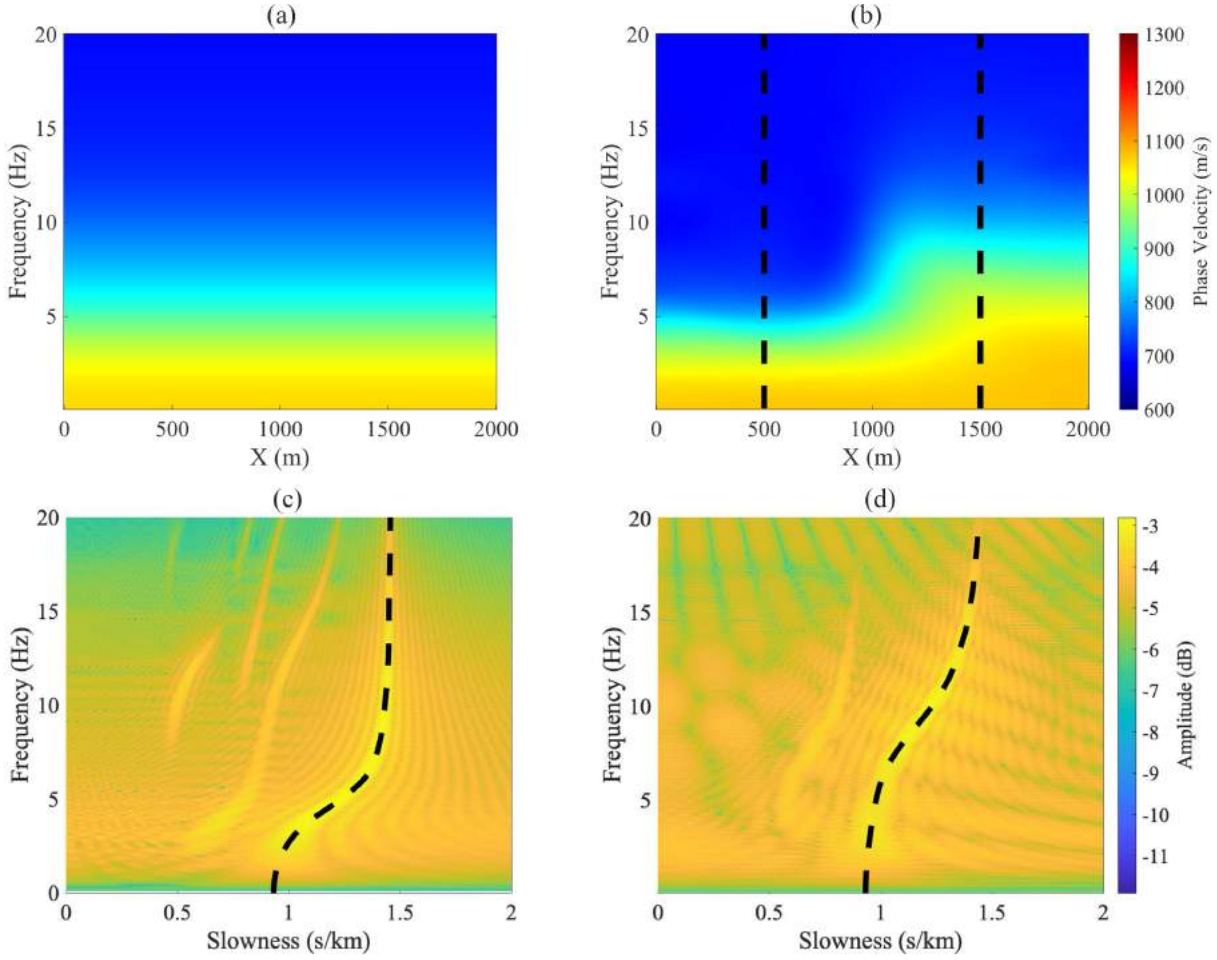

Figure 5. FWFI phase velocity results for the active source scenario. The first row displays both (a) initial and (b) final phase velocity models. The final dispersion velocity model is retrieved after 50 iterations of FWFI. The second row shows the *f*–*p* dispersion images of the two horizontally layered sections of the step velocity model overlain with dashed black velocity profiles extracted from the FWFI final model at the locations highlighted by black dashed lines. The image in (c) correspond to the thick top layer of the left-hand side of the step velocity model, whereas the one in (d) is for the thin layer in the right-hand side of the step model.

adding stronger *a priori* information (i.e. the Earth is smooth) which is therefore not justified. Hence, those models are also discarded. Finally, we also discard the combinations to the right of the black curve as the algorithm fails to estimate reasonable velocities for the low frequencies (estimates revert to the low velocity reference model). We then choose one of the remaining three combinations—the combination highlighted by a pink circle for which E is minimum among the three combinations.

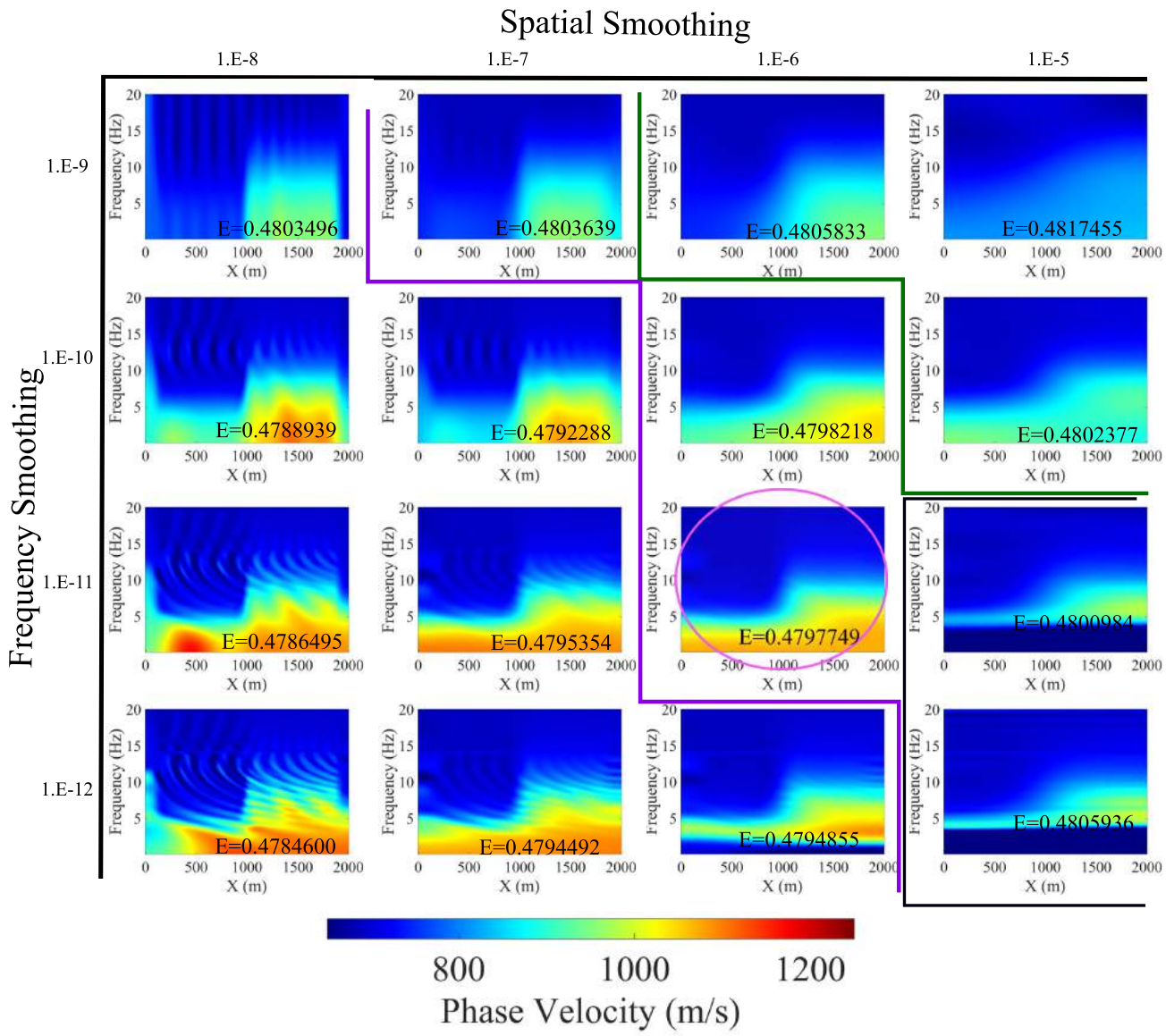

Figure 6. Velocity properties obtained using different combinations of both spatial and frequency smoothing scaling parameters ϵ_2 and ϵ_3, respectively. We choose the circled combination as it has the lowest E, data residual, among the remaining combinations. For definitions of purple, green and black curves refer to the main text.

4 AMBIENT NOISE EXAMPLE

For the ambient noise example, we use the same model as in the active source example (Figs 2a). To simulate an ambient noise response, two sources to the left and right of Fig. 2(a) are fired repeatedly with random time delays. Fig. 7 show the wavefield in both (a) space–time domain and (b) space–frequency domain and the sampling rate in both figures is 5 m. From this data set, we create different examples that simulate different acquisition scenarios to test our method. The first scenario corresponds to dense and regular spatial sampling that meets the Nyquist sampling criteria. Such dense sampling is not always viable due to logistical and environmental difficulties. Thus, in the second example, we use a data subset that is irregularly sampled. Then in a third example we use a severely aliased data subset where the sampling rate is less than the average half-wavelength. In all of the examples, we apply our method to raw noise recordings and there is no need to perform correlations to the gathers as commonly used in ambient noise seismology studies. The surface wave velocity on both left- and right-hand sides of the step in the velocity of Fig. 2(a) can be predicted analytically from the shear wave velocity for a Poisson solid medium (Stein & Wysession 2003) which produces highest and lowest possible surface wave velocities. Table 1 shows the upper and lower velocity limits, and the half of the wavelength for each frequency, data which are used to analyse the aliasing effect. Figs 8 and 9 show the input and the results of WFI and WEI for each acquisition scenario illustrated below.

4.1 Densely sampled measurements

The spatial sampling rate is 25 m and the corresponding frequencies below 14 Hz are not aliased as shown in Table 1. The input data are shown in Fig. 8(a) and the starting velocity was the same as in Fig. 5(a). Fig. 8(b) shows the reconstructed wavefield after 50

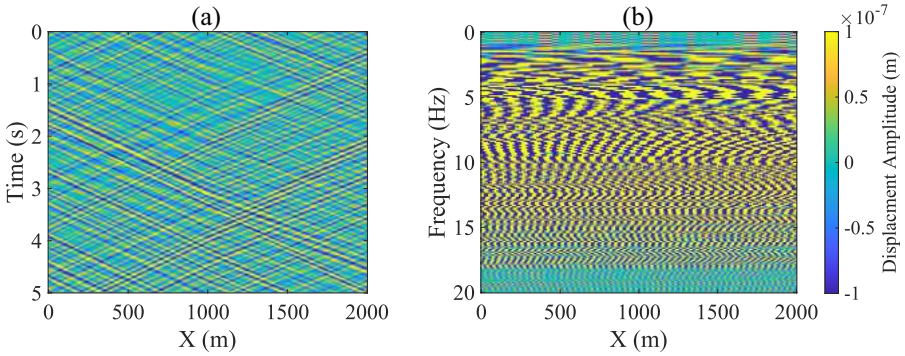

Figure 7. True-modelled ambient-noise wavefield at every 5 m in both (a) space–time domain and in (b) space–frequency domain.

Table 1. The table shows half of the wavelength for each frequency for the two limits (obtained analytically using shear wave velocities) of the surface wave velocities to analyse aliasing. The bold cells separate between aliased and unaliased frequencies, below and above the cells, respectively, for the densely sampled case with receivers at 25 m spacing.

F (Hz)	V1 ($m\,s^{-1}$)	λ/2 (m)	V2 ($m\,s^{-1}$)	λ/2 (m)
1	690	345.0	1150	575.0
3		115.0		191.7
6		57.5		95.8
9		38.3		63.9
12		28.8		47.9
15		**23.0**		38.3
18		**19.2**		31.9

iterations, now at a new spacing of 5 m in the selected spatio-frequency domain ranging spatially from 80 to 1920 m and for frequencies from 0.1 to 20 Hz. This domain is the mask that was used for both WRI and WEI which is necessary so that the source function can be neglected. Fig. 8(c) shows the difference between the true wavefield in Fig. 7(b) and the reconstructed wavefield in Fig. 8(b). Note, the difference is minimal mainly because of the presence of other modes, such as reflected and refracted body waves, in the original data set and also to interpolation numerical errors.

Fig. 9(a) shows the retrieved surface wave phase velocity after 50 iterations. At first glance, the retrieved velocity model resembles the step structure of the true velocity model. We use the same verification method as in the active source experiment where we take two velocity profiles from the retrieved phase velocity model in Fig. 9(a). As expected, the chosen velocity profiles match the dispersion obtained by *f–p* analysis of equivalent 1-D media as shown in the white dashed lines in Figs 9(d) and (e), respectively.

4.2 Irregular sampling rate

Reconstruction of a regularly sampled wavefield is an important step in our proposed method as WEI benefits from the enhanced accuracy offered by the estimated gradients. However, regular and dense samples are not always available because of field constrained and/or logistical limitations. To demonstrate the effectiveness of our method, we introduce irregular sampling of the wavefield. A randomly located sample is taken in each 40 m bin as shown in Fig. 8(d). We face then two challenges: the irregularity would introduce errors in estimating the wavefield spatial gradients; the input data are aliased for frequencies above about 9 Hz (Table 1). Nevertheless, Fig. 8(e) shows that the wavefield was successfully reconstructed, and Fig. 8(f) shows that the difference between the true and the reconstructed wavefield is acceptable. Fig. 9(d) shows the retrieved phase velocity model after 50 iterations. The velocity model is consistent with the one obtained using densely sampled data and the velocity profiles on left and right of the model match the dispersion of the fundamental mode from the *f–p* analysis as shown by the purple dashed lines in Figs 9(d) and (e), respectively.

4.3 Severely aliased data

We use a sampling rate of 175 m which creates aliasing for frequencies above 3 Hz according to Table 1. Therefore, we consider this example to be a severely aliased case to test the tolerance of our proposed inversion. The data input to the algorithm consist of the sampled wavefield shown in Fig. 8(g). The algorithm nevertheless reconstructed a reasonable wavefield estimate shown in Fig. 8(h). The difference between the true and the reconstructed wavefield is more significant than in the previous examples as shown in Fig. 8(i). Despite the low number of spatial samples in this example, FWFI managed to retrieve a decent phase velocity model after 50 iterations as shown in Fig. 9(c). The step structure is still resolved in this example and the chosen velocity profiles show a good match with the dispersion of the fundamental mode as shown by the black dashed lines in Figs 9(d) and (e).

5 DISCUSSION

The main aim of this paper is to establish a method which jointly estimates local surface wave dispersion curves and reconstructs the wavefield using the relationships between spatial and temporal gradients in the Helmholtz equation. This is performed using a two-step iterative inversion scheme where the first step reconstructs the wavefield between recorded measurements and the second uses this newly estimated wavefield to estimate the phase velocity, where we iterate between the two steps until an acceptable match to the measured wavefield is found. This approach allows local dispersion measurements to be estimated without the assumption of lateral homogeneity made in other methods such as *f–k* (Nolet & Panza 1976) or *f–p* (McMechan & Yedlin 1981) transforms. This is shown by testing the method using a step function structure; the method was able to estimate correct dispersion curves for a heterogeneous medium given a laterally homogeneous starting velocity model.

We tested our proposed method with three examples from three typical field scenarios. The reconstructed wavefield from the densely sampled data shown in the first row of Fig. 8 show that WRI reconstructs the wavefield well. Despite the fact that our approach is based on a scalar wave equation, our method was able to reconstruct

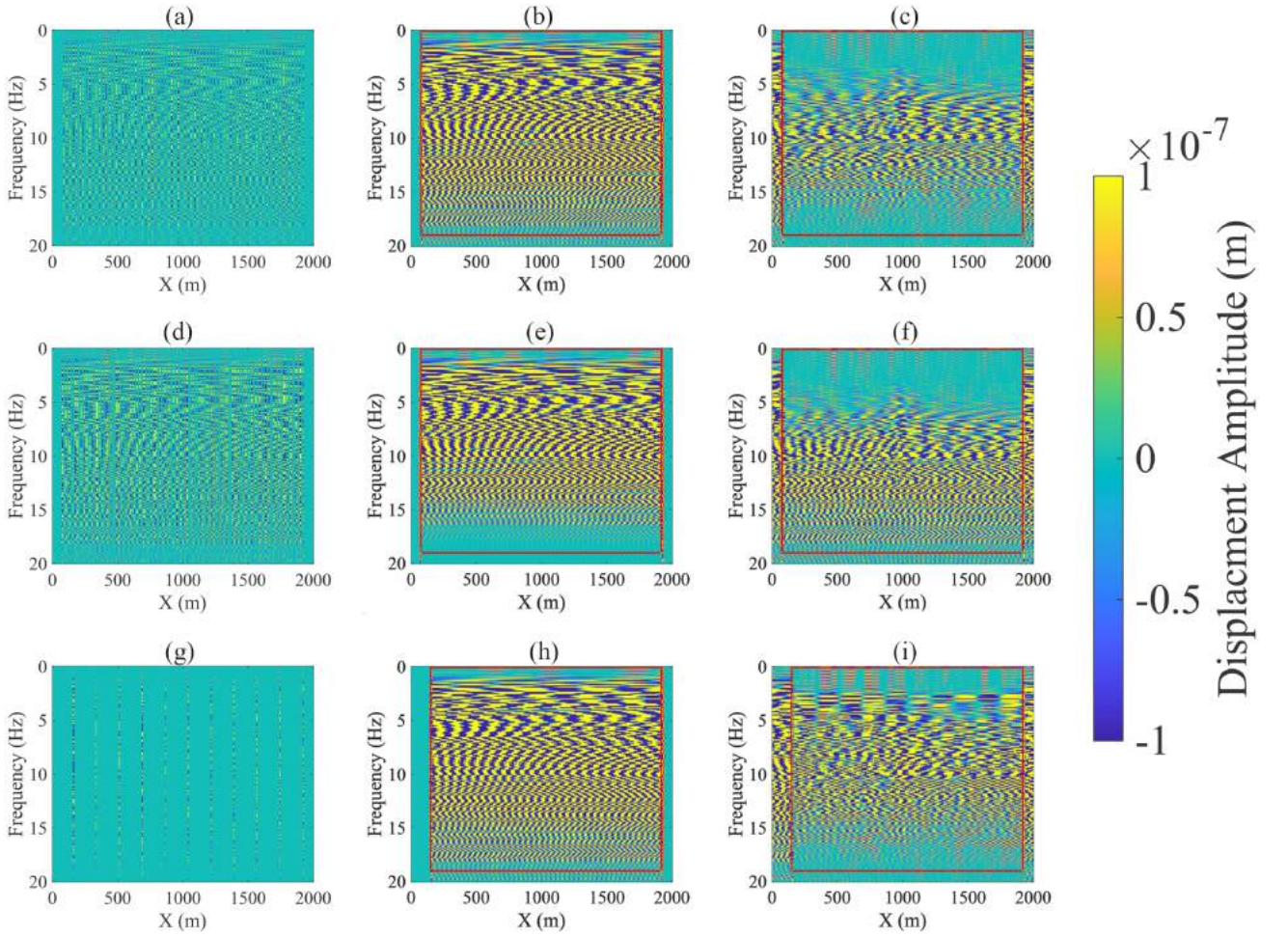

Figure 8. FWFI wavefield results of the different acquisition scenarios of the ambient noise example. (a) The data input for the non-aliased regular decimation every 25 m. (b) Wavefield estimated by FWFI after 50 iterations for the non-aliased example. (c) The difference between the reconstructed wavefield in (b) and the true wavefield shown in Fig. 7(a). (d) The data input for the irregular sampling example by selecting a random receiver every 40 m bin. (e) Wavefield estimated by FWFI after 50 iterations for the irregular sampling example. (f) The difference between the reconstructed wavefield in (e) and the true wavefield shown in Fig. 7(a). (g) The data input for the severely aliased regular decimation at every 175 m. (h) Wavefield estimated by FWFI after 50 iterations for the severely aliased example. (i) The difference between the reconstructed wavefield in (h) and the true wavefield shown in Fig. 7(a).

a wavefield that closely matches the true elastic wavefield in Fig. 7, even though other modes such as reflected and refracted *P* and *S* waves were present in the elastic data. WRI successfully reconstructed the wavefield despite the complication of irregular sampling in Fig. 8(d). This example suffers from two major challenges—errors in the finite difference estimation of gradients due to the irregularity, and mild aliasing in the data, yet the algorithm performs well. The third example showed the effectiveness of our proposed method by using the severely aliased data shown in Fig. 8(g), as the method still reconstructs a good wavefield. Fig. 8(i) shows that the difference between the true and the reconstructed wavefield is more significant than in the other examples, which could be attributed to the strong aliasing of the data. In the same manner, the step structure is resolved less well in the severely aliased data shown in Fig. 9(c) compared to the previous two scenarios. Given the extent of aliasing and under sampling of the data, we regard these results as highly encouraging. In Zhan *et al.* (2018), the simulated wavefield is based on the plane wave assumption to represent the motion of surface waves. In our examples, we used an elastic finite-difference modelling where other wave modes such as reflected and refracted *P* and *S* waves are present. The residual in the well sampled examples are related to the other modes present in the data as well as numerical errors as a result of finite difference.

When the aliasing is less significant (usually true for low frequencies only), the algorithm provides good wavefield reconstruction and estimates the correct phase velocity. This estimate, however, is bound to the starting velocity model. If the starting velocity model is close to the correct value in the aliased section of the data, then the algorithm reconstructs a good wavefield and estimates correct velocities for all frequencies. When the initial velocity is too far from the correct velocity, errors are large for the aliased part of the data but the algorithm still works well for the unaliased part of the data.

To validate the retrieved dispersive phase velocity, we compare our results to dispersion analysis of the data in the *f*–*p* domain. In Fig. 9(d) dispersion analysis is shown for the data recorded in the left-hand side of the medium and overlain with velocity profiles from the left-hand side whereas, Fig. 9(e) shows the dispersion analysis for data recorded in the right-hand side of the medium overlain with a velocity profiles extracted from the right-hand side. On both sides, the retrieved dispersion curves from the different scenarios match the dispersion of the fundamental mode. These plots showed

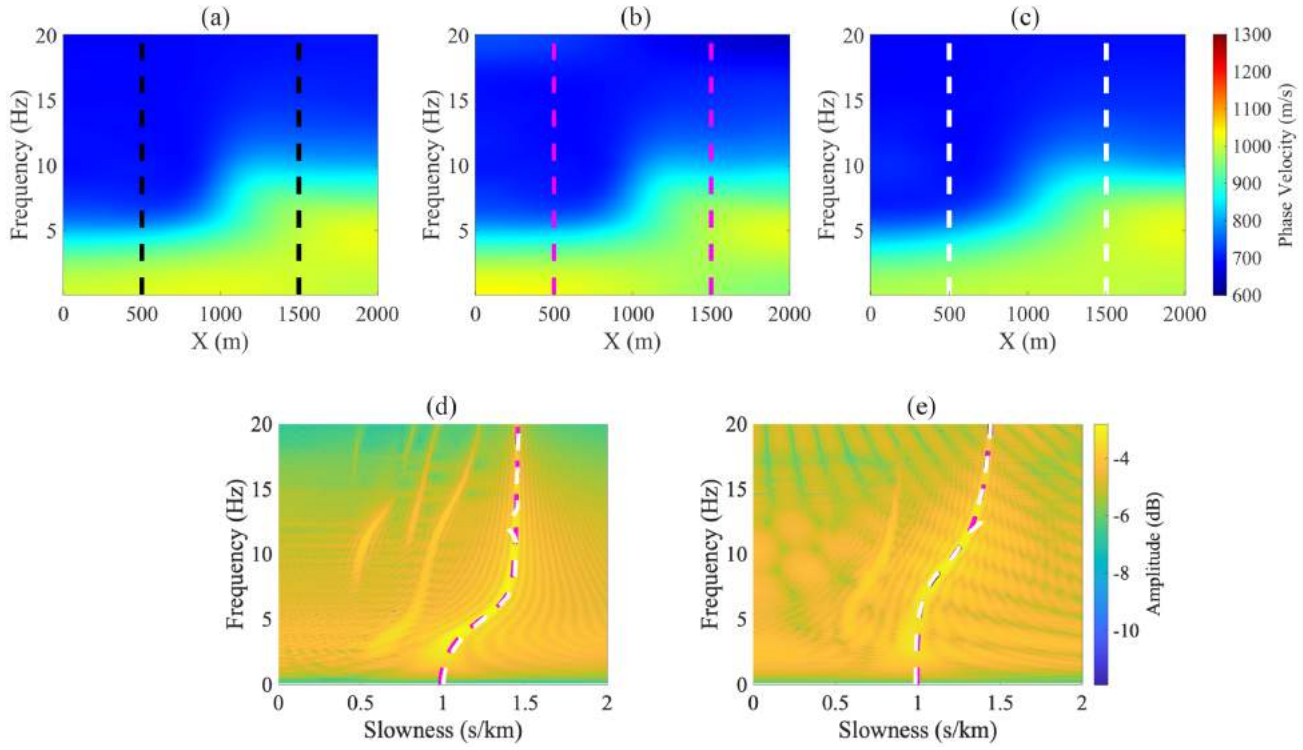

Figure 9. FWFI phase velocity results of the different acquisition scenarios of the ambient noise example. This figure shows the retrieved phase velocity model for (a) the non-aliased regular decimation every 25 m, (b) the irregular random receiver selection every 40 m bin and (c) and severely aliased regular decimation at every 175 m. The images in (d) and (e) are the *f–p* dispersion images of the two horizontally layered sections of the step velocity model overlain with dashed velocity profiles extracted from the WEI final models (all three plotted on top of one another) at the locations highlighted by their corresponding same coloured dashed lines. The image in (d) correspond to the thick top layer of the left-hand side of the step velocity model, whereas the one in (e) is for the thin layer in the right-hand side of the step model.

that FWFI was successful in obtaining the correct dispersive phase velocity model, despite using a Helmholtz scalar approximation to the elastic wavefield of the surface waves.

The extension of the method to a 2-D spatial domain would inherently add more complexity to the regularization parameters in eq. (9). Parameter ϵ_1 represents the data dependency term. In the 2-D case, this data dependency term would have to be larger than in the 1-D case as we have significantly more sets of data in 2-D, but the model space increases in size too. Updating the initial model estimate might be more challenging as finding the optimum set of regularization strengths in the 2-D case may be more difficult than the 1-D case. We anticipate that the major challenges in the application of this method to field data will be the presence of coherent and incoherent noise. Non-coherent noise could potentially be addressed by changing the norm on the data fitting term, while coherent noise could be tackled by incorporating uncertainties of the data inside a co-variance matrix in the norm. The presence of non-surface wave energy is one form of coherent noise that is successfully addressed in this study.

As future work, one might focus on the low-frequency part of the data that can be used as *a priori* information to resolve the high frequency aliased part of the data. Alternatively, the methodology may benefit from anti-aliasing processing techniques such as 5-D Antileakage Fourier Transform (Zwartjes & Sacchi 2006) to build a starting velocity model to mitigate the problem of aliasing. One extension of the proposed method is to formulate the gradiometry using an elastic wave equation rather than the acoustic wave equation used here. This would allow the methodology to account for other elastic wave modes that are present in real data. The iterative two-step optimization presented here, is one approach to solving the joint wavefield and medium parameter estimation expressed in eq. (5). In this research, we used an alternating inversion scheme where we solve the wavefield and the medium parameter separately. Valentine & Woodhouse (2010) showed that in the context of inverting for wavefield source and structural parameters, an alternating approach exhibits a poorer convergence rate than combining the two. Such a direct approach may also have benefit for solving for the wavefield and medium parameters simultaneously (i.e. a direct approach to solving eq. 5). Another extension could be to represent the wavefield using compressed sensing or using neural networks (Zhan *et al.* 2018; bin Waheed *et al.* 2021).

6 CONCLUSION

We present a wavefield inversion algorithm that images surface waves and their phase velocities. The scheme is a two-step iterative inversion that first reconstructs the full surface wavefield and then estimates the phase velocity. The scheme is driven by the wavefield gradient relationships in the Helmholtz equation. The proposed algorithm allows us to retrieve the dispersive velocity model of the medium of propagation, which in turn can be used to characterize the near-surface shear velocity structure. We tested the proposed methodology with different synthetic examples that mimic different sampling criteria including sub-Nyquist sampling rates. The results showed that wavefield reconstruction works well with irregular samples and is acceptable to a certain extent with sub-Nyquist

sampling criterion. The retrieved dispersive phase velocity compared well with an equivalent estimation of the dispersion using *f–p* method.

ACKNOWLEDGMENTS

AS would like to acknowledge Saudi Aramco for sponsoring his studies at the University of Edinburgh and allowing him to publish this research. AS thanks Nizare El Yadari for the intensive internal review of the paper.

DATA AVAILABILITY

The data underlying this article will be shared on reasonable request to the corresponding author.

REFERENCES

Aki, K., 1957. Space and time spectra of stationary stochastic waves, with special reference to microtremors, *Bull. Earthq. Res. Inst.,* **35,** 415–456.

Aki, K. & Richards, P.G., 2002. *Quantitative Seismology,* University Science Books, Sausalito, California, 2nd edn.

bin Waheed, U., Alkhalifah, T., Haghighat, E., Song, C. & Virieux, J., 2021. Pinntomo: seismic tomography using physics-informed neural networks, preprint (arXiv:2104.01588v1).

Curtis, A. & Robertsson, J.O.A., 2002. Volumetric wavefield recording and wave equation inversion for near-surface material properties, *Geophysics,* **68,** 760 , doi:10.1190/1.1567709.

Curtis, A., Trampert, J., Snieder, R.K. & Dost, B., 1998. Eurasian fundamental mode surface wave phase velocities and their relationship with tectonic structures, *J. geophys. Res. —Solid Earth,* **103,** 26919–26947.

Curtis, A., Gerstoft, P., Sato, H., Snieder, R. & Wapenaar, K., 2006. Seismic interferometry—turning noise into signal, *Leading Edge,* **25,** 1082–1092.

De Ridder, S. & Curtis, A., 2017. Seismic gradiometry using ambient seismic noise in an anisotropic earth, *Geophys. J. Int.* , doi:10.1093/gji/ggx073.

De Ridder, S. & Dellinger, J., 2011. Ambient seismic noise eikonal tomography for near-surface imaging at valhall, *Leading Edge,* **30**(5), 506–512.

De Ridder, S. A.L. & Biondi, B.L., 2015. Near-surface scholte wave velocities at ekofisk from short noise recordings by seismic noise gradiometry, *Geophys. Res. Lett.,* **42**(17), 7031–7038.

de Ridder, S. A.L. & Maddison, J.R., 2018. Full wavefield inversion of ambient seismic noise, *Geophys. J. Int.,* **215**(2), 1215–1230.

Edme, P. & Yuan, S., 2016. Local dispersion curve estimation from seismic ambient noise using spatial gradients, *Interpretation,* **4,** SJ17–SJ27.

Foti, S., Lancellotta, R., Sambuelli, L. & Socco, L.V., 2000. Notes on fk analysis of surface waves, *Ann. Geophys.,* **43**(6), 1199–1209.

Galetti, E., Curtis, A., Baptie, B., Jenkins, D. & Nicolson, H., 2016. Transdimensional love-wave tomography of the british isles and shear-velocity structure of the east irish sea basin from ambient-noise interferometry, *Geophys. J. Int.,* **208**(1), 36–58.

Jones, R.B., 1958. In-situ measurement of the dynamic properties of soil by vibration methods, *Geotechnique,* **8,** 1–21.

Langston, C.A., 2007a. Spatial gradient analysis for linear seismic arrays, *Bull. seism. Soc. Am.,* **97,** 265–280.

Langston, C.A., 2007b. Wave gradiometry in two dimensions, *Bull. seism. Soc. Am.,* **97,** 401–416.

Lehujeur, M. & Chevrot, S., 2020. Eikonal tomography using coherent surface waves extracted from ambient noise by iterative matched filtering-application to the large-n maupasacq array, *J. geophys. Res.: Solid Earth,* **125**(6), 1616–1623, doi.org/10.1029/2020JB019363.

Levshin, A., Barmin, M. & Ritzwoller, M., 2018. Tutorial review of seismic surface waves' phenomenology, *J. Seismol.,* **22**(2), 519–537.

McMechan, G.A. & Yedlin, M.J., 1981. Analysis of dispersive waves by wave field transformation, *Geophysics,* **46**(6), 869–874.

Nicolson, H., Curtis, A., Baptie, B. & Galetti, E., 2012. Seismic interferometry and ambient noise tomography in the british isles, *Proc. Geol. Assoc.,* **123**(1), 74–86.

Nicolson, H., Curtis, A. & Baptie, B., 2014. Rayleigh wave tomography of the British isles from ambient seismic noise, *Geophys. J. Int.,* **198**(2), 637–655.

Nolet, G. & Panza, G.F., 1976. Array analysis of seismic surface waves: limits and possibilities, *Pure appl. Geophys.,* **114**(5), 775–790.

Peiming, L., Kui, Z., Yimeng, Z., Zhihui, Y. & Bridle, R., 2016. Near-surface shear-wave velocity estimation based on surface-wave inversion, *Leading Edge,* **35**(11), 940–945.

Ronen, J., 1987. Wave-equation trace interpolation, *Geophysics,* **52**(7), 973–984.

Shapiro Nikolai, M., Campillo, M., Stehly, L. & Ritzwoller, M.H., 2005. High-resolution surface-wave tomography from ambient seismic noise, *Science,* **307,** 1615–1618.

Socco, L.V., Foti, S. & Boiero, D., 2010. Surface-wave analysis for building near-surface velocity models; established approaches and new perspectives, *Geophysics,* **75**(5), 75A83–75A102.

Spitz, S., 1991. Seismic trace interpolation in the fx domain, *Geophysics,* **56**(6), 785–794.

Stein, S. & Wysession, M., 2003. *An Introduction to Seismology, Earthquakes, and Earth Structure,* Blackwell, Malden, Mass., Oxford.

Tarantola, A., 1984. Inversion of seismic reflection data in the acoustic approximation, *Geophysics,* **49**(8), 1259–1266.

Trampert, J. & Woodhouse, J.H., 1995. Global phase velocity maps of love and rayleigh waves between 40 and 150 seconds, *Geophys. J. Int.,* **122,** 675–690.

Valentine, A.P. & Woodhouse, J.H., 2010. Reducing errors in seismic tomography: combined inversion for sources and structure, *Geophys. J. Int.,* **180**(2), 847–857.

van Heijst, H.J. & Woodhouse, J., 1997. Measuring surface-wave overtone phase velocities using a mode-branch stripping technique, *Geophys. J. Int.,* **131**(2), 209–230.

van Leeuwen, T. & Herrmann, F.J., 2013. Mitigating local minima in full-waveform inversion by expanding the search space, *Geophys. J. Int.,* **195,** 661–667 , doi:10.1093/gji/ggt258.

Wielandt, E., 1993. Propagation and structural interpretation of non-plane waves, *Geophys. J. Int.,* **113**(1), 45–53 , doi:10.1111/j.1365-246X.1993.tb02527.x.

Xia, J., Miller, R.D. & Park, C.B., 1999. Estimation of near-surface shear-wave velocity by inversion of rayleigh waves, *Geophysics,* **64**(3), 691–700.

Zhan, Z., Li, Q. & Huang, J., 2018. Application of wavefield compressive sensing in surface wave tomography, *Geophys. J. Int.,* **213**(3), 1731–1743.

Zhang, Z.-D. & Alkhalifah, T., 2019. Wave-equation rayleigh-wave dispersion inversion using fundamental and higher modes, *Geophysics,* **84**(4), EN57–EN65.

Zwartjes, P. & Sacchi, M., 2006. Fourier reconstruction of nonuniformly sampled, aliased seismic data, *Geophysics,* **72**(1), V21–V32.